els of Silurian soils as a result of pedoturbation, effectively increasing the average depth of soil CO_2 production.

Our results (Table 1) imply that atmospheric CO_2 declined by a factor of 10 from the Late Silurian to the Early Permian, closely following (Fig. 4) a decline predicted by theoretical carbon mass balance models (*1*). The largest decrease, between the Late Silurian and Late Devonian, coincides with a period of rapid evolution and diversification of the terrestrial ecosystem (*18*). Estimates of atmospheric CO_2 levels from geographically separated, time-equivalent paleosols are consistent, suggesting that a coherent record of changing atmospheric chemistry is preserved in the ancient soil record.

REFERENCES AND NOTES

1. R. A. Berner, *Science* **261**, 68 (1993); *Am. J. Sci.* **294**, 56 (1994).
2. T. J. Crowley and G. R. North, *Paleoclimatology* (Oxford Univ. Press, Oxford, 1991).
3. R. A. Berner and R. Raiswell, *Geochim. Cosmochim. Acta* **47**, 855 (1983); L. R. Kump and R. M. Garrels, *Am. J. Sci.* **286**, 377 (1986); R. A. Berner and D. E. Canfield, *Am. J. Sci.* **289**, 333 (1989); J. M. Robinson, *Palaeogeogr. Palaeoclimatol. Palaeoecol.* **97**, 51 (1991).
4. Geochemical proxies for measuring paleo-CO_2 are discussed by J. F. Kasting [*Nature* **355**, 676 (1992)] and R. A. Berner [*ibid.* **358**, 114 (1992)].
5. The soil carbonate paleobarometer [T. E. Cerling, *Am. J. Sci.* **291**, 377 (1991)] is based on studies of modern soils [T. E. Cerling, *Earth Planet. Sci. Lett.* **71**, 229 (1984); T. E. Cerling, J. Quade, Y. Wang, J. R. Bowman, *Nature* **341**, 138 (1989); J. Quade, T. E. Cerling, J. R. Bowman, *Bull. Geol. Soc. Am.* **101**, 464 (1989); T. E. Cerling and J. Quade, in *Climate Change in Continental Isotopic Records*, P. K. Swart, K. C. Lohmann, J. McKenzie, S. Savin, Eds., *Geophys. Monogr. Am. Geophys. Union 78* (American Geophysical Union, Washington, DC, 1993), pp. 217–232] that demonstrate that the carbon isotope composition of soil CO_2 and soil carbonate is controlled by soil productivity, the proportion of C_3 plants in the soil ecosystem, and diffusion processes and can be modeled by diffusion equations. The diffusion equations use the concentration of atmospheric CO_2 as one of the boundary conditions, so that the higher the concentration of atmospheric CO_2, the greater the impact on the isotopic composition of soil carbonate.
6. Modern soils with these features are commonly (but not exclusively) grouped under the soil order Vertisol, which require a seasonally moist, warm temperate, subtropical or tropical climate with at least 4 to 8 dry months per year [Soil Survey Staff, *Soil Taxonomy* (U.S. Department of Agriculture Handbook 436, Washington, DC, 1975)].
7. S. G. Driese and C. I. Mora, *Sedimentology* **40**, 199 (1993).
8. J. F. Mount and A. S. Cohen, *J. Sediment. Petrol.* **54**, 263 (1984).
9. We note the isotopic distinction between nodules and rhizoliths in >20 different Paleozoic red-bed vertic paleosols; the relation appears to be a general one for paleosols of vertic affinity. Pedogenic carbonate formed in soils subject to a different set of physical processes may not show this distinction.
10. Criteria for differentiating pedogenic, ground-water, and diagenetic carbonates are discussed in C. I. Mora, D. E. Fastovsky, S. G. Driese, *Studies in Geology No. 23* (University of Tennessee, Knoxville, TN, 1993).
11. T. B. Lindh, thesis, University of Miami, Miami, FL (1983); B. Popp, T. Anderson, P. Sandberg, *Bull. Geol. Soc. Am.* **97**, 1262 (1986); J. Veizer, P. Fritz, P. Jones, *Geochim. Cosmochim. Acta* **50**, 1679 (1986).
12. I. Friedman and J. R. O'Neil, *Compilation of Stable Isotope Fractionation Factors of Geochemical Interest* (U.S. Geological Survey Professional Paper 440-KK, Washington, DC, 1977).
13. An often-cited compilation [E. T. Degens, in *Organic Geochemistry: Methods and Results*, G. Eglinton and M. T. Murphy, Eds. (Springer-Verlag, Berlin, 1969), pp. 304–329] suggests a constant $\delta^{13}C$ value of –26 per mil for coals. The lack of a secular trend has been explained by physiological or biochemical regulation of plant internal pCO_2 and $\delta^{13}C$ [G. D. Farquhar, M. H. O'Leary, J. A. Berry, *Aust. J. Plant Physiol.* **9**, 121 (1982); B. N. Popp *et al.*, *Am. J. Sci.* **289**, 436 (1989)]. Carbon isotope ratios in Permian coals [P. M. Jeffery, W. Compston, D. Greenhalgh, J. de Laeter, *Geochim. Cosmochim. Acta* **7**, 255 (1955); W. Compston, *ibid.* **18**, 1 (1960)] and therapsid tooth enamel [J. F. Thackeray *et al.*, *Nature* **347**, 751 (1990)], however, indicate $\delta^{13}C$ values of about −23 per mil in the Early Permian, returning to more negative values in the Late Permian.
14. We concentrated bulk OM to 0.5 to 3 weight % by floating crushed paleosol samples in distilled water. Material that floated was composed predominantly of illite, calcite, and OM; Fe-oxides and silt-sized silicates preferentially settled. The float was washed in 10% HCl, thoroughly rinsed and dried, mixed with CuO, and combusted at 1050°C for 15 min to produce CO_2. The CO_2 was purified cryogenically before isotope ratio analysis. Eighteen of 30 paleosol samples thus prepared generated sufficient CO_2 to analyze with reproducibility of ±0.2 per mil. Standard deviation about the mean for a given time period was about ±0.5 per mil.
15. C. E. Redding *et al.*, in *Advances in Organic Geochemistry*, A. C. Douglass and J. R. Maxwell, Eds. (Pergamon, London, 1980), pp. 711–723.
16. J. M. Melillo *et al.*, *Plant Soil* **115**, 189 (1989).; D. A. Wedin, L. L. Tieszen, B. Dewey, J. Pastor, *Ecology* **76**, 1383 (1995).
17. We analyzed five samples from a 30- to 50-cm organic-rich lens within a Silurian red-bed, paleosol-bearing succession [described by P. K. Strother, *J. Paleontol.* **62**, 967 (1988)] that had qualitatively different proportions of plant-derived (*Nematothallus*) and animal-derived (cuticular fragments) OM. Only the sample most dominated by animal-derived OM differed by >0.4 per mil from a sample of plant-derived OM, which suggests that admixed animal OM will not substantially alter the $\delta^{13}C$ of bulk OM in a soil.
18. W. N. Stewart, *Paleobotany and the Evolution of Plants* (Cambridge Univ. Press, New York, 1983); P. G. Gensel and H. N. Andrews, *Plant Life in the Devonian* (Praeger, New York, 1984); *Am. Sci.* **75**, 478 (1987).
19. S. G. Driese *et al.*, *J. Sediment. Petrol.* **62**, 825 (1992).

20. We thank the donors of The Petroleum Research Fund grant 25678-AC8 and of the NSF grants EAR-9206540 and EAR-9418183.

12 September 1995; accepted 1 December 1995

Initial Results of Radio Occultation Observations of Earth's Atmosphere Using the Global Positioning System

E. R. Kursinski,* G. A. Hajj, W. I. Bertiger, S. S. Leroy, T. K. Meehan, L. J. Romans, J. T. Schofield, D. J. McCleese, W. G. Melbourne, C. L. Thornton, T. P. Yunck, J. R. Eyre, R. N. Nagatani

Recent radio occultation measurements using Global Positioning System satellite transmitters and an orbiting receiver have provided a globally distributed set of high-resolution atmospheric profiles, suggesting that the technique may make a significant contribution to global change and weather prediction programs. Biases in occultation temperatures relative to radiosonde and model data are about 1 kelvin or less in the tropics and are generally less than 0.5 kelvin at higher latitudes. Data quality is sufficient to quantify significant model errors in remote regions. Temperature profiles also reveal either an equatorial Rossby-gravity or an inertio-gravity wave. Such waves provide a fundamental source of momentum for the stratospheric circulation.

Radio occultation is a technique for sounding the structure of atmospheres from space with high accuracy and vertical resolution. Since the mid-1960s, it has been used by planetary spacecraft to measure vertical density, pressure, and temperature structure in the atmospheres of Venus, Mars, and the outer planets (*1–4*). With the completion of the constellation of 24 orbiting radio transmitters known as the Global Positioning System (GPS), the sensitivity and coverage necessary to improve upon existing data sets for the Earth's atmosphere in a simple, cost-effective manner are now available. Here we present initial temperature and water vapor profile data derived from measurements made in April and May 1995 during the prototype GPS occultation mission, GPS-MET, launched in April 1995 (*5*). These profiles are compared with radiosonde (balloon) data and atmospheric anal-

E. R. Kursinski, Division of Geological and Planetary Sciences and Jet Propulsion Laboratory, California Institute of Technology, Pasadena, CA 91125, USA.
G. A. Hajj, W. I. Bertiger, S. S. Leroy, T. K. Meehan, L. J. Romans, J. T. Schofield, D. J. McCleese, W. G. Melbourne, C. L. Thornton, T. P. Yunck, Jet Propulsion Laboratory, California Institute of Technology, Pasadena, CA 91109, USA.
J. R. Eyre, United Kingdom Meteorological Office, Bracknell, Berkshire RG12 2SZ, UK.
R. N. Nagatani, Climate Prediction Center/COB, Washington, DC 20233, USA.

*To whom correspondence should be addressed.

yses available every 6 hours from the European Center for Medium-Range Weather Forecasts (ECMWF) (6). A comparison made between about 150 retrieved temperature profiles in the Northern Hemisphere and the ECMWF analysis indicates that, between altitudes of 5 and 30 km, GPS occultation temperature profiles are accurate to better than 1 K in the mean with a standard deviation of 1 to 2 K. Theoretical predictions suggest that GPS radio occultation is capable of <1 K accuracy below 35 km, with a vertical resolution of ≤ 1 km and a horizontal resolution of ≤ 200 km, and is insensitive to clouds and aerosols (*7–9*). With a potential 500 occultations per day per orbiting receiver, the technique provides a unique combination of well-distributed global coverage and high vertical resolution, particularly in the troposphere.

In radio occultation, the atmosphere acts as a planetary-scale lens. Signals from a transmitter that pass through the atmosphere are deflected by the vertical gradient of atmospheric refractive index and are then detected by an orbiting receiver (Fig. 1). The bending angle α varies with the impact parameter a as the orbital motion of the transmitter and receiver cause the tangent height of the ray path to descend through the atmosphere. The vertical refractive index profile $n(r)$ is derived from measurements of $\alpha(a)$ with an Abel integral transform, subject to the assumption of local spherical symmetry (*1*). Temperature profiles are obtained from $n(r)$ with the use of empirical data on the variation of refractive index with atmospheric properties (*10*). Bending angle $\alpha(a)$ is calculated from receiver measurements of the Doppler frequency of the occulted beam, given precise knowledge of the positions and velocities of the transmitter and receiver (*11*).

Below an altitude of 90 km, the primary contributors to radio wavelength refractivity, defined as $N(r) = [n(r) - 1] \times 10^6$, are dry atmospheric density and water vapor density. Throughout the middle atmosphere and the regions of the troposphere colder than 250 K, the contribution of water vapor to refractivity is small, and measured refractivity profiles can be converted directly into density profiles, which are then integrated hydrostatically to determine pressure. Given density and pressure, temperature is obtained from the ideal gas law. Temperature errors resulting from the 50% uncertainties in climatological water vapor at the 250 K level are less than 1 K (*8, 12, 13*). On the basis of noise considerations, the hydrostatic integral is initialized at 50 km in the temperature retrievals presented below, and a temperature estimate at 50 km is required as a boundary condition. This temperature, derived from a model, is the only independent atmospheric information used in the retrieval process when the atmosphere is dry. A 10 K error in the 50-km temperature estimate produces a temperature error of about 0.1 K at the 100-mbar level ($\sim$16 km).

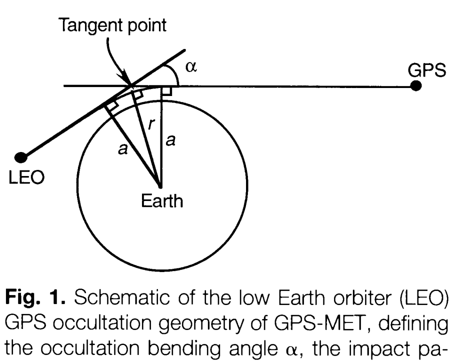

Fig. 1. Schematic of the low Earth orbiter (LEO) GPS occultation geometry of GPS-MET, defining the occultation bending angle α, the impact parameter a, and the radius to the ray periapsis tangent point, r.

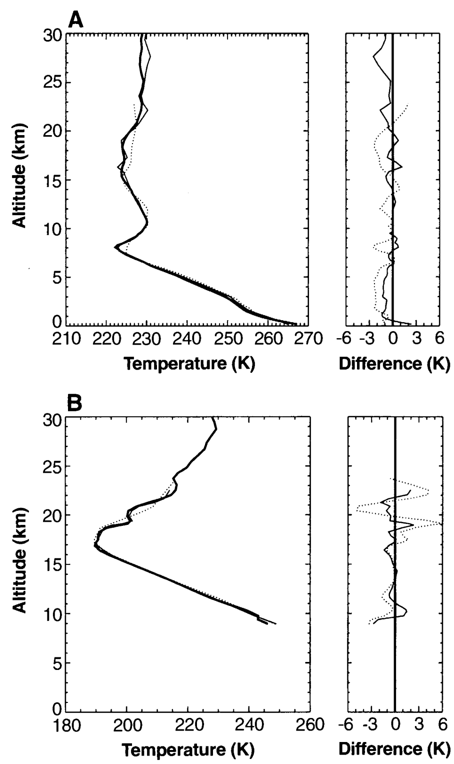

Fig. 2. Comparisons between occultation (thick line), radiosonde (thin line), and ECMWF (dotted line) temperature profiles. (Left panels) Comparisons of the profiles. (Right panels) Temperature differences (occultation-radiosonde or model) as a function of altitude. (**A**) Occultation obtained at 01:33 universal time (UT) on 5 May 1995 over Hall Beach, Northwest Territories, Canada (69.2°N, 82.6°W). The radiosonde (00:00 UT; 68.8°N, 81.3°W) was 65 km from the occultation location, and the model analysis from 00:00 UT is spatially interpolated to the occultation location. (**B**) Occultation obtained at 12:40 UT on 4 May 1995 in the south Pacific (7.9°S, 167.5°E). The radiosonde profile (12:00 UT; 6.0°S, 170.4°E), obtained from a ship, was 350 km from the occultation location, and the model analysis from 12:00 UT is spatially interpolated to the occultation location.

Retrieved occultation temperature profiles can be evaluated by comparing specific examples with radiosonde and ECMWF model profiles (Fig. 2). At high latitudes, cold, dry conditions allow accurate temperatures to be derived almost to the surface (Fig. 2A). The retrieved profile is similar to the nearby radiosonde profile, with differences of order 1 K through most of the troposphere. In the vicinity of the tropopause and above, temperature differences are comparable to those between the radiosonde and model analysis. Agreement with the radiosonde in resolving the sharply defined tropopause and the lapse rate change below 3 km is illustrative of the sensitivity and vertical resolution of the occultation technique. At low latitudes, the ability of the technique to measure the high and cold tropopause structure characteristic of the tropics is illustrated (Fig. 2B).

Figure 2B also illustrates the sensitivity of radio occultation to atmospheric waves (*3, 14*). Waves are most apparent in the equatorial lower stratosphere. Although other waves are present throughout this region, one of $\sim$3-km vertical wavelength appears in a number of profiles within 10° of the equator above the Pacific with a vertical structure antisymmetric about the equator. Close agreement in both amplitude and phase with a radiosonde sounding taken some 300 km away (Fig. 2B) implies that the wave has been resolved by the occultation measurement and that the horizontal wavelength is large ($\gg$300 km). Although a large-scale inertio-gravity wave cannot be ruled out, these features, the wave's absence in a profile at 0.3°N latitude, and an amplitude that has largely decayed by the 10-mbar level ($\sim$30 km) are consistent with a 4- to 5-day westward propagating Rossby-gravity wave, one of the two dominant planetary wave types observed previously in this region (the other is a 10- to 20-day Kelvin wave) (*15*). These waves may be

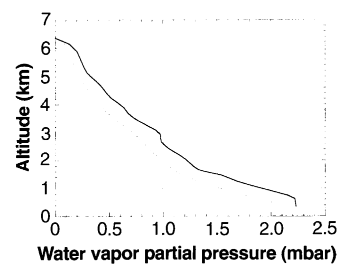

Fig. 3. Comparison of the occultation (solid line) and radiosonde (dashed line) water vapor profiles for the occultation over Hall Beach (Fig. 2A). The radiosonde temperature profile is used to remove the dry density contribution from the occultation refractivity profile in order to isolate the water vapor component. The water vapor retrieval is initialized at about 6.2 km in altitude, where water vapor abundance is assumed to be zero.

generated by tropical convection and provide significant sources of energy and momentum for the stratospheric circulation. The location of the wave is consistent with a convective source over the warm pool region around Indonesia.

As temperatures rise above 250 K lower in the troposphere, water concentrations increase dramatically. This introduces an ambiguity in the interpretation of refractivity but also allows water vapor to be retrieved given independent temperature data (Fig. 3) (*13, 16*). The retrieved water vapor in Fig. 3 is biased high by 0.1 to 0.4 mbar relative to the radiosonde because of systematic differences between the retrieved and radiosonde refractivity profiles. Biases of a similar magnitude are expected at low latitudes, giving relative accuracies an order of magnitude better. Unfortunately, the vertical structure often associated with higher water concentrations at lower latitudes causes large variations in the occulted signal that the GPS-MET receiver cannot adequately track. Results for temperatures warmer than 250 K are therefore not generally presented here. Receiver modifications to improve low-altitude signal tracking are in progress. At low latitudes, the vertical resolution, insensitivity to clouds, and coverage of GPS occultations are needed to address fundamental issues in hydrology, weather, and climate and are lacking in present satellite sensors (*17*).

To evaluate the accuracy of our temperature profiles, given the rarity of close coincidences with radiosondes, we compared them with the ECMWF analyses (Fig. 4). Tropospheric temperatures exceeding 250 K were excluded. In the Northern Hemisphere troposphere, where the ECMWF analyses are the most accurate, mean temperature differences are generally less than 0.5 K, and the standard deviations of the differences are of order 1 K. These differences include vertical structure that is not resolved by the ECMWF analysis, especially above the 100-mbar level.

Although radiosonde and TIROS Operational Vertical Sounder (TOVS) (*18*) data are assimilated into the ECMWF model, the analyses are less accurate in some regions of the Southern Hemisphere because of the sparse distribution of radiosondes. Greater knowledge of the structure of the atmosphere over the Southern Hemisphere oceans is essential for studies of climate and the global energy and water cycles. Because the occultation retrieval process has little dependence on latitude, these temperature measurements can be used to characterize atmospheric structure in the Southern Hemisphere in more detail. In the Southern Hemisphere, mean temperature differences and standard deviations increase at lower altitudes (Fig. 4C). This feature was produced by 12 occultation profiles concentrated far from radiosonde ascents, primarily in the southeastern Pacific in the Southern Hemisphere storm track and close to the ice edge, where problems in the assimilation of TOVS data are known to arise (*19*). The statistics for these 12 profiles, when compared with those of the remaining 38 Southern Hemisphere profiles, reveal a bimodal signature in model accuracy (Fig. 5). Biases and standard deviations of the temperature differences of the 38 profiles (Fig. 5A) are generally comparable to those in the Northern Hemisphere (Fig. 4A). In contrast, the 12 profiles (Fig. 5B) show that the model tropopause altitude is 1 to 2 km too low, and model temperature is ~2 K too low in the troposphere and ~3 K too high in the lower stratosphere. These differences are larger than the predicted decadal climate variations and imply that caution is appropriate when model data are used to establish climatological behavior and to study climatic changes in regions devoid of high vertical resolution observations. The temperature biases and errors in tropopause height, which must be significant given the importance of the height and topography of the tropopause to tropospheric dynamics (*20*), suggest that GPS occultation measurements can improve medium-range weather forecasts in regions where weather systems move from remote oceans onto continents.

Temperature differences at tropical latitudes also display distinctive structure (Fig. 4B). On average, retrieved profiles are colder than the ECMWF analyses between 300 and 70 mbar, with a maximum difference of about 1 K near 150 mbar, whereas above the 70-mbar level, they become warmer by a similar amount. Retrieved temperature gradients between 80 and 60 mbar are therefore systematically larger than model gradients. Although a little warmer than the retrievals, radiosonde data exhibit similar temperature structure in this altitude range, suggesting that the model does not have sufficient resolution to represent these gradients. Because equatorial waves in the lower stratosphere are not resolved by the model, they are probably responsible for the increase in standard deviation above the 100-mbar level in Fig. 4B.

The source of the temperature biases in the upper tropical troposphere (Fig. 4B) is not understood. These biases could affect the available convective potential energy in the troposphere, and therefore energy transfer within the atmosphere and the severity of convective storms. They could also affect radiative emission by cirrus clouds, an important component of the greenhouse effect, and troposphere-stratosphere exchange through the thermal control of water vapor transfer. Given the preliminary nature of these results, the biases seen in Fig. 4B could be a product of occultation measurement error. However, the good agreement between the retrievals and model in the Northern Hemisphere (Fig. 4A) argues against this. Errors in the model data are attributable primarily to incomplete model physics and

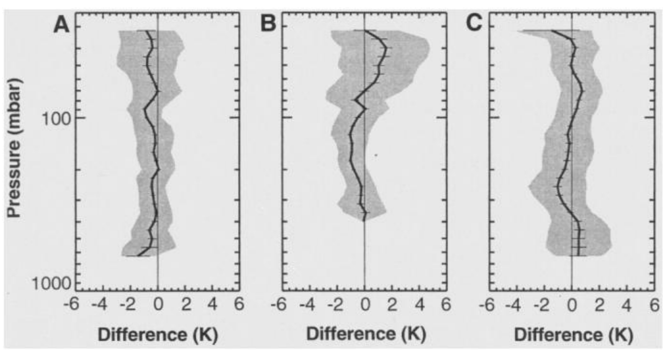

Fig. 4. Statistical comparisons between the 6-hour ECMWF analyses and temperature profiles retrieved from radio occultations on 4 and 5 May 1995. The panels plot mean temperature differences (retrieved − ECMWF) for (**A**) 54 profiles in the Northern Hemisphere (>30°N), (**B**) 52 profiles in the tropics (30°S to 30°N), and (**C**) 50 profiles in the Southern Hemisphere (>30°S). The vertical curve represents mean temperature differences, and the horizontal error bars depict the standard error in the mean. The shaded area is defined by the mean temperature difference plus or minus the standard deviation of the temperature difference about the mean. In the Northern and Southern hemispheres, the troposphere-stratosphere boundary (tropopause) typically lies in the 250- to 300-mbar range, whereas in the tropics, it is near the 100-mbar level.

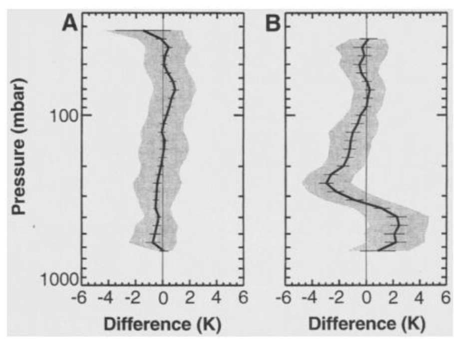

Fig. 5. Statistical comparison of the 50 Southern Hemisphere profiles, divided into two groups: (**A**) 38 profiles that differ little relative to the model and (**B**) the 12 profiles with the largest deviations relative to the model. Bars and shading as in Fig. 4.

imperfect radiosonde observations. Model physics becomes important when the model extrapolates to locations and times far from the ground truth provided by radiosondes. However, radiosonde temperatures are themselves imperfect and require corrections for absorption of solar and infrared radiation, thermal emission, and conduction and convection of heat (*21*). Inadequate calibration could contribute to the temperature biases seen in Fig. 4B, to the extent that the model is constrained by radiosondes in this region.

Figures 2 through 5 indicate that future measurements, if available in near real-time, could play a significant role in numerical weather prediction (NWP). The density of 500 globally distributed measurements per day provided by a single orbiting GPS receiver would exceed that of the radiosonde network by a factor of 2 in the Southern Hemisphere, making a significant contribution to the global observing system. A constellation of orbiting receivers could make a major contribution to fulfilling the stated temperature observation requirements for global NWP. The results presented here demonstrate desirable properties for use in NWP, namely generally good agreement with a high-quality NWP analysis, plus the ability to identify a minority of cases where there is room for significant improvement in the analysis.

REFERENCES AND NOTES

1. G. F. Fjeldbo, V. R. Eshleman, A. J. Kliore, *Astron. J.* **76**, 123 (1971).
2. G. F. Lindal, *J. Geophys. Res.* **84**, 8443 (1979); A. J. Kliore and I. R. Patel, *ibid.* **85**, 7957 (1980).
3. D. P. Hinson and J. A. Magalhaes, *Icarus* **94**, 64 (1991).
4. G. F. Lindal, *Astron. J.* **103**, 967 (1992).
5. Atmospheric radio occultation observations using a GPS receiver in low Earth orbit were proposed and developed for the National Aeronautics and Space Administration's (NASA's) Earth Observing System in 1988 (*22*), but the concept became a reality with the launch of the University Corporation for Atmospheric Research (UCAR) GPS-MET experiment on 3 April 1995 (*23*).
6. A. C. Lorenc, *Mon. Weather Rev.* **109**, 701 (1981); D. B. Shaw, P. Lonnberg, A. Hollingsworth, P. Unden, *Q. J. R. Meteorol. Soc.* **113**, 533 (1987).
7. E. R. Kursinski, G. A. Hajj, K. R. Hardy, in *Proceedings of the 8th Symposium on Meteorological Observations and Instrumentation*, Anaheim, CA, 17 to 22 January 1993 (American Meteorological Society, Boston, MA, 1993), pp. J153–J158.
8. ______, *Proceedings of the SPIE Symposium on Optical Engineering and Photonics in Aerospace Science and Sensing, Paper 1935-13* (1993).
9. K. R. Hardy, G. A. Hajj, E. R. Kursinski, *Int. J. Satell. Commun.* **12**, 463 (1994).
10. G. D. Thayer, *Radio Sci.* **9**, 80 (1974).
11. To obtain the accuracies necessary for atmospheric work, we used a modified version of the GIPSY–OASIS II system developed at the Jet Propulsion Laboratory for the Ocean Topography Experiment (TOPEX/Poseidon) to determine receiver and transmitter orbits, and to calibrate and remove receiver and transmitter clock biases and instabilities (*9, 24*). Vertical smoothing, decreasing from ~1.4 km in the stratosphere to ~0.5 km near the surface, was also applied to the Doppler frequency measurements to make them consistent with the Fresnel diffraction resolution limit (*3, 7*). Finally, unwanted dispersive ionospheric contributions to bending were removed by forming a linear combination of the bending angles estimated independently for each of the two GPS signal frequencies (*25*).
12. G. A. Hajj, E. R. Kursinski, W. I. Bertiger, L. J. Romans, K. R. Hardy, in *Proceedings of the 7th Conference on Satellite Meteorology and Oceanography*, Monterey, CA, 6 to 10 June 1994 (American Meteorological Society, Boston, MA, 1994), pp. J7–J10.
13. E. R. Kursinski, G. A. Hajj, K. R. Hardy, L. J. Romans, J. T. Schofield, *Geophys. Res. Lett.* **22**, 2365 (1995).
14. D. P. Hinson and G. L. Tyler, *Icarus* **54**, 337 (1983); D. P. Hinson and J. A. Magalhaes, *ibid.* **105**, 142 (1993); D. P. Hinson and J. M. Jenkins, *ibid.* **114**, 310 (1995).
15. D. G. Andrews, J. R. Holton, C. B. Leovy, *Middle Atmosphere Dynamics* (Academic Press, Orlando, FL, 1987).
16. E. R. Kursinski, G. A. Hajj, K. R. Hardy, *Eos* **72**, 372 (1991); M. Bevis *et al.*, *J. Geophys. Res.* **97**, 15787 (1992); L. L. Yuan *et al.*, *ibid.* **98**, 14925 (1993).
17. D. O'C. Starr and S. H. Melfi, *NASA Conf. Publ. 3120* (May 1991).
18. W. L. Smith, H. M. Woolf, C. M. Hayden, D. Q. Wark, L. M. McMillan, *Bull. Am. Meteorol. Soc.* **60**, 1177 (1979).
19. J. R. Eyre, G. A. Kelly, A. P. McNally, E. Andersson, A. Persson, *Q. J. R. Meteorol. Soc.* **119**, 1427 (1993).
20. B. J. Hoskins, M. E. McIntyre, A. W. Robertson, *ibid.* **111**, 877 (1985).
21. J. K. Luers and R. E. Eskridge, *J. Appl. Meteorol.* **34**, 1241 (1995).
22. T. P. Yunck, G. F. Lindal, C. H. Liu, *Proceedings of IEEE Positioning, Location, and Navigation Symposium*, Orlando, FL, 29 November to 2 December 1988, pp. 251–258.
23. R. Ware *et al.*, *Bull. Am. Meteorol. Soc.* in preparation.
24. W. I. Bertiger *et al.*, *J. Geophys. Res.* **99**, 24449 (1994).
25. V. V. Vorob'ev and T. G. Krasil'nikova, *Izv. Akad. Nauk SSSR Fiz. Atmos. Okeana* **29**, 626 (1993).

26. The research described here was largely performed at the Jet Propulsion Laboratory, California Institute of Technology, supported jointly by NASA and the California Institute of Technology through the Caltech President's fund. We are grateful to our collaborators, GPS-MET principal investigator R. Ware and project manager M. Exner, of the UCAR, Boulder, CO, for providing us with access to raw flight data from the GPS-MET experiment. We also thank the ECMWF for providing us with atmospheric data, software, and assistance with data interpretation and M. E. Gelman of the National Meteorological Center (NMC) for many useful discussions on the NMC radiosonde data set.

11 September 1995; accepted 28 December 1995

Observations of Carbon Monoxide in Comet Hale-Bopp

David Jewitt,* Matthew Senay,* Henry Matthews

The recently discovered comet Hale-Bopp (C/1995 O1) sports a bright dust coma even though it is still far from the sun (presently 6 astronomical units). This feature has attracted considerable interest in the public and scientific arenas. The comet is headed toward perihelion at 0.92 astronomical unit in April 1997 and is widely expected to then become a spectacular naked-eye comet. With millimeter-wave observations, carbon monoxide (CO) has been identified as the driver for the early activity observed in Hale-Bopp.

Activity in comets near the sun is known to be driven by the sublimation of water ice from the nucleus in response to strong solar heating (*1*). Comet Hale-Bopp belongs to a class of comets that are too distant and too cold for water ice to sublimate, raising the possibility that the activity creating its dust coma is driven by the sublimation of a more volatile ice or even by another physical process. Historically, activity in distant comets has been attributed to heat released by exothermic phase changes in water ice, explosive reactions between radicals in the nucleus, collisions with interplanetary boulders, or the outgassing of embedded supervolatiles such as carbon monoxide, carbon dioxide, and nitrogen. The advent of sensitive millimeter-wave telescopes allows us to search directly for outgassed supervolatiles.

We first observed Hale-Bopp in September 1995 using the 15-m-diameter James Clerk Maxwell Telescope (JCMT) atop Mauna Kea, Hawaii. We studied the J = 2-1 rotational transition of CO at 230 GHz. At the time of observation, Hale-Bopp was at a heliocentric distance of 6.6 astronomical units (AU). Nearby position and flux standards were also observed, from which we estimated a pointing accuracy of ±2 arc sec. The diameter of the circular JCMT beam subtended 20 arc sec on the sky (corresponding to 9.3×10^7 m at the comet), which is large compared with the pointing uncertainties.

The comet appeared projected against the center of our galaxy (Fig. 1), producing a nonuniform background of diffuse emission from interstellar CO along the line of sight. Cometary CO emission was detected on 5 and 7 September 1995 [universal time (UT)] but appeared partially confused with background CO lines and noise because of

D. Jewitt and M. Senay, Institute for Astronomy, Honolulu, HI 96822, USA.
H. Matthews, Joint Astronomy Centre, Hilo, HI 96720, USA, and Herzberg Institute of Astrophysics, Ottawa, ON K1A 0R6, Canada.

*Visiting Astronomer at the James Clerk Maxwell Telescope, operated by the Royal Observatory, Edinburgh, on behalf of the Particle Physics and Astronomy Research Council of the United Kingdom, the Netherlands Organization for Scientific Research, and the National Research Council of Canada.